ADVANCED ELECTRONIC MATERIALS
www.advelectronicmat.de

X-ray Detectors With Ultrahigh Sensitivity Employing High Performance Transistors Based on a Fully Organic Small Molecule Semiconductor/Polymer Blend Active Layer

Adrián Tamayo, Ilaria Fratelli, Andrea Ciavatti, Carme Martínez-Domingo, Paolo Branchini, Elisabetta Colantoni, Stefania De Rosa, Luca Tortora, Adriano Contillo, Raul Santiago, Stefan T. Bromley, Beatrice Fraboni, Marta Mas-Torrent,* and Laura Basiricò*

The implementation of organic semiconductor (OSC) materials in X-ray detectors provides exciting new opportunities for developing a new generation of biocompatible devices with high potential for the fabrication of sensitive and low-cost X-ray imaging systems. Here, the fabrication of high performance organic field-effect transistors (OFETs) based on blends of 1,4,8,11-tetramethyl-6,13-triethylsilylethynyl pentacene (TMTES) with polystyrene is reported. The films are printed employing a low cost and high-throughput deposition technique. The devices exhibit excellent electrical characteristics with a high mobility and low density of hole traps, which is ascribed to the favorable herringbone packing (different from most pentacene derivatives) and the vertical phase separation in the blend films. As a consequence, an exceptional high sensitivity of $(4.10 \pm 0.05) \times 10^{10}$ μC Gy^{-1}cm^{-3} for X-ray detection is achieved, which is the highest reported so far for a direct X-ray detector based on a tissue equivalent full organic active layer, and is higher than most perovskite film-based X-ray detectors. As a proof of concept to demonstrate the high potential of these devices, an X-ray image with sub-millimeter pixel size is recorded employing a 4-pixel array. This work highlights the potential exploitation of high performance OFETs for future innovative large-area and highly sensitive X-ray detectors for medical dosimetry and diagnostic applications.

1. Introduction

The capacity of X-rays to traverse optically opaque substances with little absorption has led to their widespread use in modern society. X-ray detectors are key to high-resolution imaging systems employed in many fields such as diagnostic healthcare, astrophysics, industrial inspection, security, and cultural heritage preservation.[1] The demand for low X-ray dose detection, high sensitivity and cost-efficient devices has resulted in to the development of new X-ray detectors based on responsive semiconductors. Such detectors rely on the generation of electron-hole pairs from incoming radiation, which can be measured by an electrical readout.[2] The main virtue of these detectors is their outstanding combination of high speed, spatial resolution, and sensitivity.

Current X-ray detectors use inorganic semiconductors (e.g., amorphous-Se, amorphous-Si, poly-CdZnTe (CZT),

---

A. Tamayo, C. Martínez-Domingo, M. Mas-Torrent
Institut de Ciència de Materials de Barcelona (ICMAB-CSIC) and
Networking Research Center on Bioengineering
Biomaterials and Nanomedicine (CIBER-BBN)
Campus de la Universitat Autònoma de Barcelona
Cerdanyola, Barcelona E-08193, Spain
E-mail: mmas@icmab.es

I. Fratelli, A. Ciavatti, B. Fraboni, L. Basiricò
Department of Physics and Astronomy
University of Bologna and National Institute for Nuclear Physics – INFN
section of Bologna
Viale Berti Pichat 6/2, Bologna 40127, Italy
E-mail: beatrice.fraboni@unibo.it

The ORCID identification number(s) for the author(s) of this article can be found under https://doi.org/10.1002/aelm.202200293.

DOI: 10.1002/aelm.202200293

P. Branchini, E. Colantoni, S. De Rosa, L. Tortora
Surface Analysis Laboratory INFN Roma Tre
Via della Vasca Navale 84, Rome 00146, Italy

P. Branchini, E. Colantoni, S. De Rosa, L. Tortora
INFN
Roma Tre, via della Vasca Navale 84, Rome, Italy

E. Colantoni
Department of Mathematics and Physics
Roma Tre University
via della Vasca Navale 84, Rome, Italy

L. Tortora
Department of Sciences
Roma Tre University
Via della Vasca Navale 84, Rome, Italy

A. Contillo
Elettra-Sincrotrone Trieste
Area Science Park Strada Statale 14, km 163.5, Trieste, Basovizza, 34149, Italy

R. Santiago, S. T. Bromley
Departament de Ciència de Materials i Química Física & Institut de
Química Teòrica i Computacional (IQTCUB)
Universitat de Barcelona
Barcelona, Spain

diamond). However, these materials present severe limitations for the growing need for curved and large area image detectors with reduced image distortion and vignetting. To overcome these technological issues, the use of organic semiconductors (OSCs) in X-ray detectors has several advantages, such as light weight, compatibility with flexible substrates and low-cost solution processability (e.g., by roll-to-roll production).

The inherent low atomic number (Z) of OSCs, mimicking that of human tissue, meets the requirements for medical dosimetry applications. These materials are suitable for detectors with a wide dynamic range and for low energy X-rays and, hence, are highly promising for medical applications in the so-called "mammography energy range," <40 KeV.[3] For applications requiring high attenuation for hard X-rays (>40 KeV), composite films have also been introduced comprising high-Z elements integrated into an OSC, such as lead-halide perovskites, nanoparticles or quantum dots containing heavy elements.[4–11] However, the manufacturing of these materials requires complicated processes and still remains a challenge. Moreover, the introduction of high absorbing elements limits the tissue equivalence of OSCs, also introducing a higher toxicity level, e. g. due to the presence of lead in the most commonly used perovskites. Therefore, the implementation of novel OSC materials in X-ray detectors provides exciting new opportunities for developing a new generation of biocompatible devices with high potential for the fabrication of sensitive and low-cost X-ray imaging systems.

Recently, organic X-ray detectors based on organic field-effect transistors (OFETs) have successfully been reported.[12,13] High-energy photon absorption is challenging in organic materials since they are constituted of atoms with low Z atomic numbers. Hence, semiconductors with high-Z atoms included into their basic molecular structure, such as the benchmark OSC bis-(triisopropylsilylethynyl)pentacene (TIPS-pentacene), have been used as active materials to increase radiation capture, while preserving tissue equivalence.[14] In our previous work, p-type OFETs using blends of TIPS-pentacene with polystyrene (PS) were reported to exhibit an unprecedented X-ray sensitivity for organic-based direct detectors, and matching that of perovskite thick films.[13] The OSC films were prepared by a high throughput solution shearing technique (i.e., bar-assisted meniscus shearing, BAMS)[15–18] that gives rise to large area crystalline films. Our findings concluded that the detector performance is strongly affected by both i) the grain size and grain boundaries and ii) the device mobility. Regarding the former, films with lower crystal domains revealed a higher performance due to an increase in the density of traps for minority charge carriers (i.e., electrons in TIPS-pentacene) that assist the photoconductive gain effect. On the other hand, the device mobility can be optimized by using OSCs thin films crystallizing in structures exhibiting high intermolecular electronic coupling and by minimizing the trap density for majority charge carriers (i.e., holes in TIPS-pentacene). The latter is strongly reduced by using OSC:PS blends since during the thin film deposition a vertical phase separation takes place resulting in a bottom PS layer that passivates the interfacial charge traps.[19]

With the aim at further improving the X-ray detector performance, we pursued the fabrication of OFETs showing an enhanced hole transport. Specifically, in this work, blends of PS with the OSC 1,4,8,11-tetramethyl-6,13-triethylsilylethynyl pentacene (TMTES) were investigated. The molecular structure of this material is very similar to TIPS-pentacene, however, the Bar-Assisted Meniscus Shearing (BAMS) deposited thin films crystallize in a totally different crystal packing (i.e., a herringbone packing motif). This resulted in OFETs that reached very high mobilities of up to 2.5 $cm^2\ V^{-1}\ s^{-1}$ and showed a reduced density of interfacial hole traps thanks to the previously mentioned phase separation of the blend. As a consequence, an exceptional high sensitivity of $(4.10 \pm 0.05) \times 10^{10}$ $\mu C\ Gy^{-1}\ cm^{-3}$ for X-ray detection was achieved, surpassing by one order of magnitude TIPS-pentacene detectors. This sensitivity value is the highest reported so far for a direct X-ray detector based on a tissue equivalent full organic active layer. As a proof of concept to demonstrate the high potential of these devices and thanks to the outstanding X-ray sensitivity of TMTES, an X-ray image with sub-millimeter pixel size was recorded employing a 4-pixel array.

2. Results

Thin films of TMTES and blends of TMTES:PS were prepared using the BAMS technique under ambient conditions (**Figure 1**a). The use of blends of small molecule semiconductors with insulating polymers has shown to facilitate semiconductor processability and to lead to thin films with an enhanced crystallinity, electrical performance and device stability.[20–24] PS was chosen as binding polymer due to its low relative permittivity, good solubility in organic solvents, low cost and the fact that interacts weakly with OSCs. Solutions of 2.0% w/w in chlorobenzene were employed. In the case of blends, the best thin film characteristics were achieved using a TMTES:PS (PS of 280 KDa) with a ratio 2:1 and a coating speed of 10 mm s^{-1} (Table S1, Supporting Information). All the inks were deposited at 105 °C (a temperature compatible with flexible electronic applications) on Si/SiO_2 substrates with interdigitated gold electrodes treated with a self-assembled monolayer of 2,3,4,5,6-pentafluorobenzenethiol (PFBT) (see Experimental Section). It has been observed that the PFBT monolayer promotes nucleation and improves the device reproducibility. The prepared films were isotropic, highly homogenous, and crystalline and exhibited an excellent device-to-device reproducibility with almost 100% yield.

The polarized optical microscopy (POM) images of the films are shown in Figure 1b. All the films show polycrystalline spherulitic domains without a clear preferential orientation of the crystals. This morphology is similar to the one previously observed in TIPS-pentacene films.[13,16,25,26] It can be noticed that the grains are smaller in the channel area than on the SiO_2 regions far from the electrodes, which can be ascribed to the gold PBFT treatment that promotes nucleation.[27–29]

TMTES and TMTES:PS thin films were further characterized by atomic force microscopy (AFM), as shown in **Figure 2**a,b. All the films showed step edges of around 1.7 ± 0.1 nm, which is in agreement with the length of an extended molecule (inset Figure 2a). A low roughness of 6.5 ± 1.2 nm and 7.0 ± 3.8 nm for TMTES and TMTES:PS, respectively, was observed. Further, the thicknesses of

S. T. Bromley
Institució Catalana de Recerca i Estudis Avançats (ICREA)
Barcelona, Spain

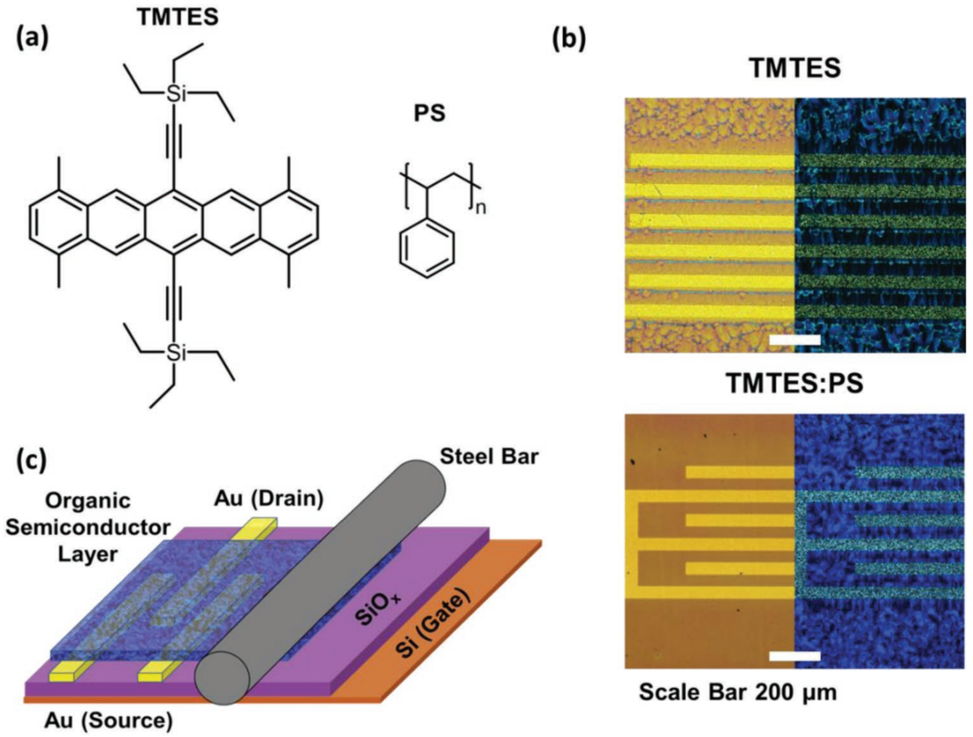

Figure 1. BAMS deposition of TMTES and TMTES:PS thin films. a) Molecular structures of TMTES and PS. b) Optical microscope images (left) and cross-polarized optical microscope images (right) of TMTES and TMTES:PS thin films deposited by BAMS on a Si/SiO$_2$ substrate with pre-patterned interdigitated gold electrodes. c) Scheme of the BAMS technique for the deposition of the active layer.

TMTES and TMTES:PS films were found to be 22 ± 6 nm and 32 ± 7 nm, respectively (Figure S1, Supporting Information).

The chemical maps of TMTES and TMTES:PS films obtained by Time-of-Flight Secondary Ion Mass Spectrometry (ToF-SIMS) are reported in Figure S2a,b (Supporting Information). The characteristic molecular ion fragment originating from TMTES ($SiC_3H_9^+$ $m/z = 73.05$) was used to monitor the distribution of the semiconductor over an area of 500 µm × 500 µm. The ion signal of TMTES appears uniformly distributed all over the surface for the blended TMTES:PS film, indicating that there is no horizontal phase segregation. The different surface morphologies of the two films is visible in the 3D surface height profiles maps, obtained by the stylus profilometer (Figure S2c,d, Supporting Information). In order to study the vertical distribution of the insulating polymer, ToF-SIMS depth profiling of TMTES:PS film was investigated (Figure 2c). The four representative profiles of TMTES, PS, PBFT, and the SiO$_2$ substrate were obtained averaging the signal intensities of the characteristic secondary ions. These ions are generated from the different stratified materials constituting the OFET channel area. The behaviour of characteristic fragments from TMTES and PS confirm the co-presence of the organic semiconductor (OSC) and the insulator. As we inspect deeper in the film towards the substrate, the PS ion signals evolve separately from the ones of the (OSC) appreciating a well-defined TMTES-PS transition region. At this point, the signal coming from TMTES decreases significantly, while PS signal increases. Further, the signal shape of PFBT shows an additional layer between the PS and the Si/SiO$_2$ substrate, that represents the experimental evidence of the effective electrode functionalization carried out to improve charge injection and the semiconductor crystallisation.[30–32] In Figure 2d, the 3D ToF-SIMS map reconstruction of the overlayed signals from thin film profile are reported. These measurements are in agreement with previous results[16,22,33–35] and demonstrate that PS is acting as a dielectric passivating layer.

Two different TMTES polymorphs are reported in the literature. TMTES films deposited from solution (i.e., drop casting, spin coating) have been described to crystallize into the same phase as the previously resolved single crystal structure, hereafter named Polymorph I (PI).[36,37] This polymorph crystallizes forming a slip-stack structure. On the other hand, more recently, TMTES microcrystals grown from solution and analyzed by transmission electron microscopy were found to exhibit a new structure (i.e., Polymorph II or PII), in which the molecules stack in a herringbone motif.[38] X-ray diffraction measurements performed in the here-prepared films reveal that, in all the cases explored, TMTES crystallizes in the PII phase (**Figure 3**a; Figure S3, Supporting Information). Additionally, the observation of only the (*00l*) reflection peaks confirms that the crystals are oriented with the *ab* plane parallel to the substrate, which is the most favorable scenario for charge transport, as detailed below.

Polymorphism is known to have a strong impact on device performance.[39–42] In order to compare the hole transport tendencies of the two TMTES polymorphs, we analyzed all independent pairwise HOMO-HOMO (Highest Occupied Molecular Orbital) intermolecular electronic couplings (J_{HOMO}) in the two crystal structures using Density Functional Theory (DFT) based calculations (Figure 3b and **Table 1**). For polymorph

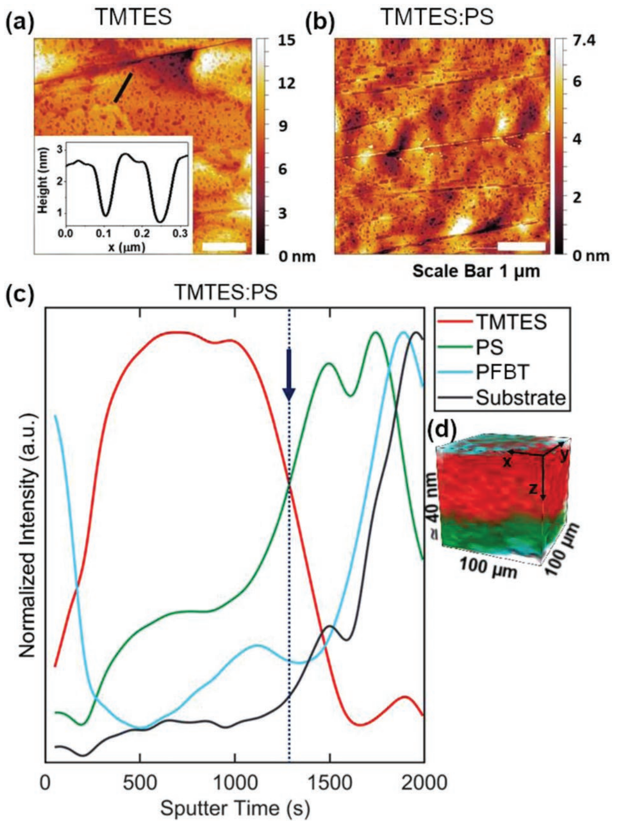

Figure 2. AFM topography images of TMTES (a) and TMTES:PS (b) thin films. The inset in (a) corresponds to the height profile along the black line in the figure. c) ToF-SIMS study of the TMTES:PS thin films. Normalized (to maximum) ToF-SIMS depth profile acquired in the channel area of the OFET starting from the surface and reaching the SiO_2 substrate (black curve). The TMTES signal (red curve) includes the SiC^-, $SiCH^-$, SiC_2H^-, $SiC_5H_2^-$, $SiC_7H_2^-$ species; the PS signal (green curve) includes the $C_3H_3^-$, $C_4H_3^-$, $C_5H_3^-$, $C_6H_3^-$, $C_7H_3^-$ species; the PBFT signal (light blue curve) includes the F^- and S^- species. d) 3D rendering of the same species of the (c) panel, as the sputter time is proportional to Z-profiling of the layers. The analyzed thickness (40 ± 12 nm) was multiplied by a factor $2.5\,10^4$ to better appreciate the multilayer architecture in the 3D rendering. Dashed line and arrow indicate the TMTES-PS transition region.

TMTES-PI, we find a highly anisotropic one dimensional (1D) electronic structure with only a single dominant J_{HOMO} value of 105 meV along the *a*-axis. On the other hand, TMTES-PII exhibits stronger intermolecular intra-stack couplings (J_{HOMO} = 172 meV) with also significant inter-stack electronic couplings. The electronic interactions in PII thus span across the whole *ab* plane, indicative of a 2D electronic isotropy, which is more desirable for charge transport.[43–45]

All the films were electrically characterized as active layers in OFETs under ambient conditions. Table S1 (Supporting Information) collect the electrical parameters extracted for all the devices and **Figure 4** shows the transfer and output characteristics of representative OFETs based on the two formulations. All the OFETs based on TMTES (i.e., without PS binding polymer) exhibit an average mobility of 0.10 ± 0.03 $cm^2\,V^{-1}\,s^{-1}$ and a high positive threshold voltage (V_{TH}) of 27 ± 9 V. The latter is indicative of some unintentional doping of the semiconductor, which might be ascribed to the penetration of water toward the dielectric interface. In contrast, OFETs based on TMTES:PS as active layer show an improved device performance. The devices operate with a much lower voltage window (5 V) and exhibit excellent electrical characteristics with lower hysteresis and a much lower mobility dependence with the gate voltage (Figure S4, Supporting Information). The V_{TH} of these devices are closer to 0 V (in the range -0.5 to -1 V), further proving that the use of PS is beneficial for the processing of the OSC in environmental conditions.[15,20,22,23] Also, a low density of traps for majority charge carriers (i.e., holes) of (3.9 ± 0.9) $10^{11}\ eV^{-1}\,cm^{-2}$ was estimated from the sub-threshold slope, which is one order of magnitude lower than the value found for the films without

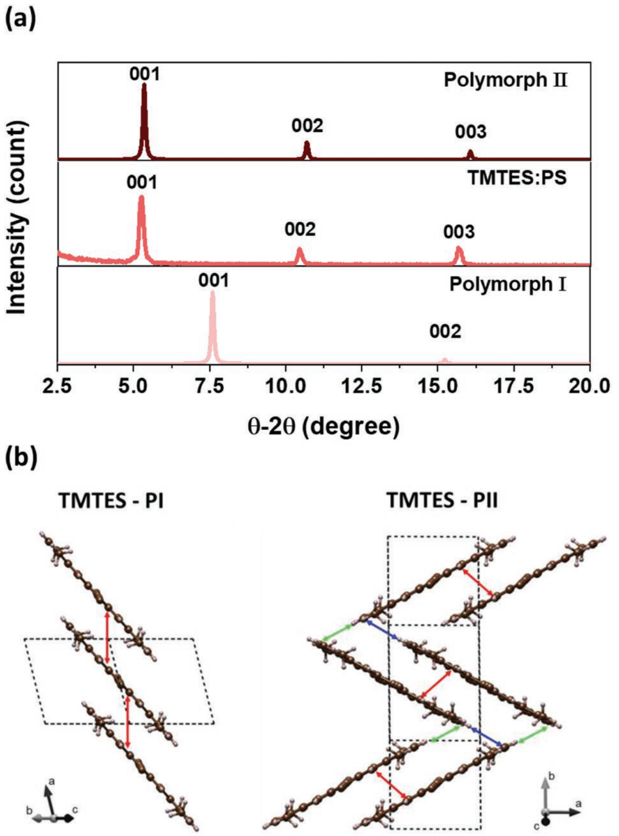

Figure 3. a) X-ray diffractogram of a representative TMTES:PS film together with the simulated diffractograms of the reported polymorphs in the (*00l*) plane. b) Crystal packing of TMTES polymorphs PI and PII. The arrows of each color indicate non-equivalent interactions between pairs of molecules in each polymorph respectively.

Table 1. Transfers integrals calculated for non-equivalent dimer interactions in the two polymorphs TMTES-PI and TMTES-PII. The color-coding of the dimer interaction numbers corresponds to the colored arrows in Figure 3, indicating different interactions between pairs of molecules.

	Dimer interaction	J_{HOMO} [meV]
TMTES PI	1	105
TMTES PII	1	172
	2	17
	3	17

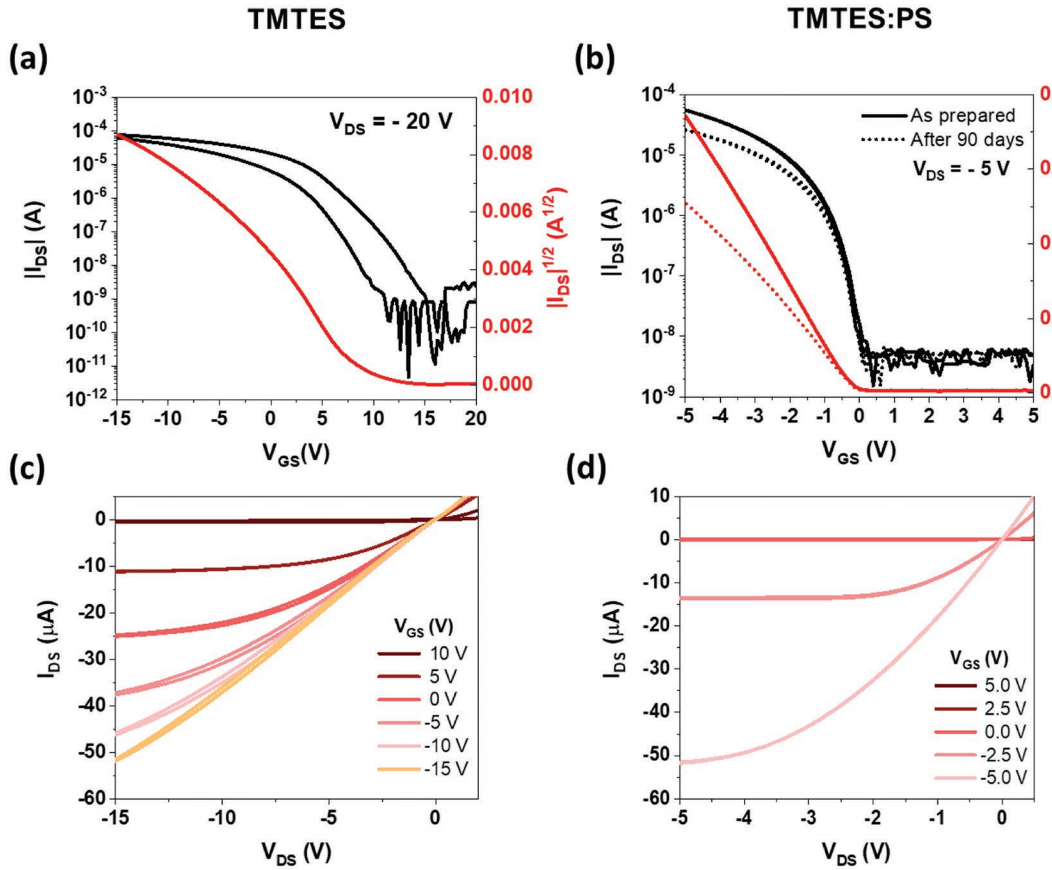

Figure 4. Electrical performance of the OFET devices. Transfer characteristics in saturation regime of representative a) TMTES and b) TMTES:PS based OFETs. For the blended films, the device characteristics after 90 days are shown (dashed lines). Output characteristics of representative c) TMTES and d) TMTES:PS based OFETs.

PS ((6.3 ± 1.1) 10^{12} eV^{-1} cm^{-2}). This finding is in agreement with previous results and confirms that the passivation of the dielectric with PS is responsible for the reduction of interfacial traps. Additionally, the shelf-stability of the TMTES:PS devices showed a mobility decay less than 50% after 90 days. On the contrary, TMTES OFETs reveal poor time stability, as reflected mainly by a very high positive threshold voltage shift after the same period of time (Figure S5, Supporting Information). In addition, bias stress measurements of TMTES:PS OFETs were carried out under ambient conditions at constant bias voltage V_{GS} of -10 V and V_{DS} of -1 V between transfer characteristics measurements (Figure S6, Supporting Information). After 5 h of measurements, the TMTES:PS OFETs underwent a shift in the V_{TH} of 1.4 V and the saturation mobility only decreased 15% of its initial value.

The TMTES:PS based devices showed a high average mobility of 2.6 ± 0.6 cm^2 V^{-1} s^{-1} (maximum mobility found: 3.1 cm^2 V^{-1} s^{-1}). Further, the measured anisotropy ratio, that is the ratio between the mobility of the films with channel length parallel and perpendicular to the coating directions ($\mu\|/\mu\perp$), was estimated to be in the range 1.4–1.2 for TMTES films and 1.1–1.3 for the TMTES:PS ones (Table S1, Supporting Information). Such mobility values and electrical characteristics found for the TMTES:PS films are among the best values reported for this semiconductor (see Table S2, Supporting Information).[36,37,46–48] It should be also highlighted that the films previously reported were fabricated by means of lab-scaled solution deposition techniques (such as spin-coating and drop casting), while in this work the films are fabricated employing a low-cost high throughput technique compatible with roll-to-roll processes, a strong added-value for mass production.

OFETs based on the parent compound TIPS-pentacene fabricated following the same methodology (i.e., blended with PS and deposited by BAMS, hereafter TIPS:PS) led to device mobilities in the range 0.5-1 cm^2 V^{-1} s^{-1} and a density of traps of (9.2 ± 2.8) 10^{11} eV^{-1} cm^{-2}.[13,16,26,49] In comparison, TMTES films show a field-effect mobility between two and four times higher, that we ascribe to the more favorable 2D herringbone crystal packing and also to the lower presence of interfacial hole-traps.

The superior transport properties of TMTES:PS films deposited by BAMS have been exploited to realize organic thin film direct X-ray detectors exhibiting ultrahigh sensitivity to the radiation. During irradiation the devices have been biased to work in the saturation regime (V_{DS} = –15 V and V_{GS} = –20 V) and the current flowing between the source and drain electrodes have been measured through multiple on/off beam switching cycles. The real-time current response to irradiation at different dose rates showed the typical photoconversion dynamic processes found in organic microcrystalline thin films (see Figure S7, Supporting Information). These are ruled by a photoconductive gain effect, assisted by traps for minority carriers present in the organic semiconducting layer, that allows effective and highly sensitive detection of high energy photons in tissue equivalent, low absorbing material systems such as full-organic thin films.[12] According to this detection mechanism, the photocurrent gain is defined as the ratio between two characteristic times: the lifetime of the minority charge carriers (i.e., electrons in our case) trapped in the material (τ_r) and the transit time of the majority charge carriers (i.e., holes in our case) along the channel (τ_t). The transit time is affected by the efficacy to the charge transport within the channel since it is inversely dependent from the mobility of majority charge carriers ($\tau_t = L^2/\mu V$, where L is the channel length and V is the applied bias). The sensitivity of the detector depends linearly on the gain and can be thus boosted by acting both on the electron trap density (e.g., by tuning the grain boundary density) and on the optimization of the hole transport in the active layer (e.g., by optimizing the OSC structure/crystallinity and the OSC/dielectric interface by passivating the holes traps).[13] The X-ray sensitivity value has been calculated as the slope of the X-ray induced photocurrent in function of the impinging dose rate, as reported in **Figure 5**a. We achieved sensitivity to X-rays up to (4.10 ± 0.05) 10^{10} μC Gy^{-1} cm^{-3}, which represents not only the highest value reported so far for a fully-organic tissue equivalent

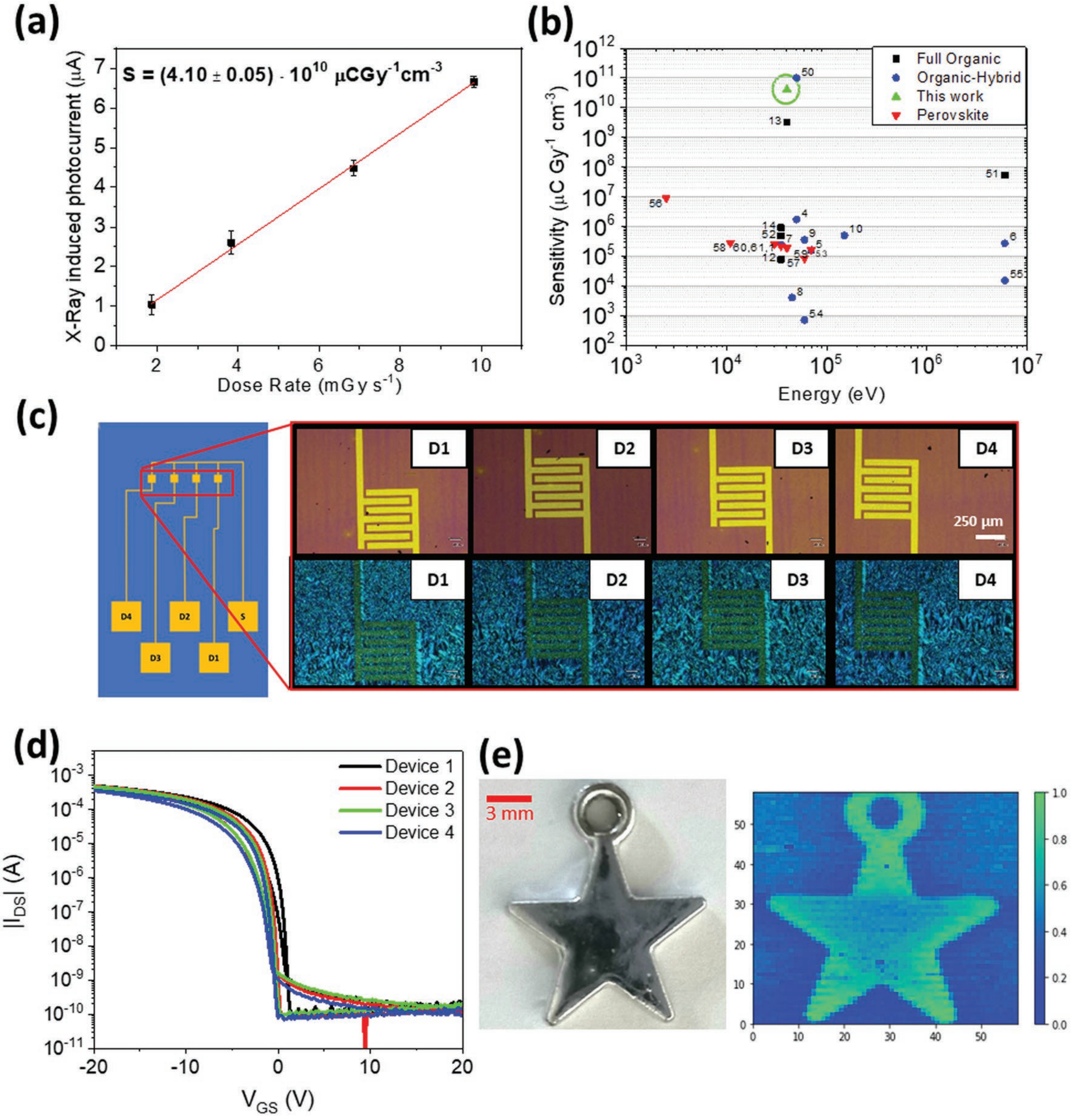

Figure 5. X-ray detection of TMTES:PS film-based devices. a) X-ray induced photocurrent as a function of the dose rate. The sensitivity is estimated as the slope of the linear fit of the experimental points and resulted in the top value reported in inset. b) Comparison of the sensitivity values per unit volume achieved in this work (green triangle), with those reported at the state of the art for thin-film detectors based on perovskite (red triangles), organic-hybrid (blue circles), and full-organic (black squares) active layers.[1,4–10,12–14,50–61] c) Layout and POM images of the 4 pixels array BAMS printed TMTES:PS detector. d) OFET transfer characteristics of the 4 pixels of the array. e) Photograph (right) and corresponding X-ray image by a single pixel device (left) of an aluminium object.

active layer, but it is also higher than most perovskite film-based X-ray detectors, as shown in Figure 5b. Considering that our active layer is composed of very thin films (i.e., a few tens of nanometers), we also plotted the corresponding graph of the sensitivity values per unit area in Figure S8 (Supporting Information). Further, the here-reported sensitivity value is only slightly lower than that recently reported for similar photon energies for hybrid organic-perovskite thin film X-ray detectors[50] deposited by spin coating, i.e., not a scalable process. We note that the employment of lead-halide perovskite in the active layer limits the tissue-equivalence of the sensing material. Having a human tissue equivalence absorbance of the ionizing radiation represents a strong added value of our reported device, allowing unique opportunities in medical dosimetry application. We ascribe the outstanding detection performance of TMTES:PS thin film to their excellent transport properties, achieved thanks to the fabrication of highly crystalline thin films combined with their high electrical stability due the passivation role of PS.

As a proof of concept of the reliability of our devices as large area detectors for medical application we realized an array of 4 pixels and tested them at the SYRMEP (Synchrotron Radiation for Medical Physics) beamline of the ELETTRA light source (Trieste, Italy). SYRMEP was chosen since it is designed for research in biomedical imaging with X-ray energy range (8.5–35 keV) and dose rates (0.05–35 mGy s^{-1}), well suited for diagnostic mammography. The homogeneous coating achieved by means of the BAMS technique is testified by similar morphologies shown by POM images, and overlapping OFETs transfer characteristics of the 4 pixels, reported in **Figure 5**c,d, respectively. The X-ray projection image of a star-shaped metal object (Figure 5d) shows high contrast and assesses the good reproducibility of the detector performance over a total of 3600 expositions at the same experimental conditions, with a lateral resolution of 250 µm, limited by the device dimension and the X-ray beam collimation. It is noteworthy that thanks to the very high X-ray sensitivity of TMTES, it was possible to employ a sub-millimeter pixel size, in a range very appealing for large-area portable X-ray panels.[62]

3. Conclusions

Thin films of the OSC TMTES and TMTES blended with PS were prepared employing a high throughput printing technique. The thin films crystallize in a herringbone motif that exhibit 2D electronic interactions. The OFETs fabricated with the blended films exhibited excellent device performance and stability compared to the OFETs based on the pristine OSC. Accordingly, TMTES:PS based OFETs exhibited a threshold voltage close to zero, low operation voltage and an average mobility of 2.6 cm^2 V^{-1} s^{-1}. Further, the density of hole traps was significantly reduced when using the PS due to the vertical phase separation taking place during the crystallization, that leads to the passivation of the dielectric.

The OFET devices were then investigated as X-ray detectors. An unprecedented X-ray sensitivity was achieved for an organic electronic device up to $(4.10 \pm 0.05) \times 10^{10}$ µC Gy^{-1} cm^{-3}, which was even higher than most perovskite film-based X-ray detectors. As a proof of concept, an array of four pixels was employed for imaging a metallic object in an X-ray beamline designed for medical radiographies. In conclusion, this work highlights the potential exploitation of high performance low-cost OFETs employing human-tissue equivalent organic materials as active layers, for future innovative large-area and highly sensitive X-ray detectors for medical dosimetry and diagnostic applications.

4. Experimental Section

Materials and Device Fabrication: 1,4,8,11-Tetramethyl-6,13-triethylsilylethynyl pentacene (TMTES) and polystyrene (PS) of 10 000 and 280 000 g mol^{-1} were purchased from Ossila and Sigma–Aldrich, respectively, and used without further purification. The TMTES and PS solutions were prepared in anhydrous chlorobenzene with a final concentration of 2.0% w/w: For the blend solutions, the TMTES and PS solutions were mixed in a TMTES:PS volume ratio of 2:1. Before deposition, the solutions were heated at the substrate temperature used for the coating process.

Interdigitated gold electrodes were patterned by photolithography on heavily *n*-doped Si wafer (Si-Mat) with a 200 nm thick layer of SiO$_2$. Five nanometers of Cr (acting as adhesion layer) followed by 40 nm of Au were thermally evaporated on the Si wafer. The channel lengths (L) varied from 25 to 200 µm and the channel width/length ratio were always set constant to 100 (W/L). The substrates were then cleaned by sonication with acetone and isopropanol in HPLC grade and then dried under nitrogen flow.

The surface of the source and drain electrodes were chemically modified with a self-assembled monolayer of 2,3,4,5,6-pentafluorothiophenol (PFBT, from Sigma–Aldrich). The gold surfaces were exposed to an ultraviolet ozone cleaner for 25 min and then immersed in a 15×10^{-3} M solution of PFBT in isopropanol for 15 min. Finally, the substrates were washed with pure isopropanol to remove the PFBT excess and dried under nitrogen flow.

The TMTES solutions were then deposited by Bar- Assisted Meniscus Shearing (BAMS) following the previously reported methodology.[15–17] The BAMS deposition was carried out at a substrate temperature of 105 °C and with a coating speed of 1 and 10 mm s^{-1}. Note that all the fabrication process was carried out under ambient conditions and no post-thermal treatments were required.

Thin Film Characterization: The optical microscopy images were taken using an Olympus BX51 equipped with polarizer and analyzer. Surface topographies of the thin films were examined by a 5500LS Scanning Probe Microscopy system from Agilent Technologies and subsequent data analysis was performed by using Gwyddion 2.56 software.

X-ray diffraction measurements were carried out with a PANalytical X'Pert Pro MRD (Materials Research Diffractometer) diffractometer. The Cu K-alpha radiation 1.54187 Å was used.

Time-of-flight secondary ion mass spectrometry (ToF-SIMS) measurements were performed using a TOF SIMS V instrument (ION-TOF GmbH, Muenster, Germany). The base pressure of the analysis chamber during the ToF-SIMS data acquisition was $\approx 1.3 \times 10^{-9}$ mbar. Bi$_3^{++}$ primary ions at 30 keV provided by a liquid metal ion gun (LMIG) were used for surface analysis. For depth profiling in dual-beam mode, the analysis beam was combined with a sputter ion gun producing Cs$^+$ ions at 500 eV. The analysis area of the surface chemical maps was 500 µm × 500 µm. Sputtering was carried out over 300 µm × 300 µm areas inside the OFET active layer. Depth profiles were acquired over 100 µm × 100 µm areas within the centre of the sputter crater. The analysis beam (pulse width: 18.4 ns, current: ≈0.3 pA) and the sputtering beam (current: ≈6 nA) were employed in non-interlaced mode (1 analysis frame, 1 s sputter and 1 s pause per cycle) for sample charge compensation. Secondary ions were extracted at 2 kV and detected with a time-of-flight mass analyzer. A cycle time of 100 µs allowed to obtain a mass range from 1 to 900 m/z. The detected secondary ions had negative and positive polarity. Negative and positive mass spectra were calibrated using CH^-, Si^-, C_5^-, and $C_{42}H_{50}Si_2^-$, and H^+, CH^+, CH_3^+, and $C_{42}H_{50}Si_2^+$ signal peaks, respectively. The mass resolution ($m\ \Delta m^{-1}$) achieved is better of 6000 for all analyzed masses. Mass spectra and depth profile signals were exported for further analysis by SurfaceLab v6.5 software. A list of characteristic secondary ions was obtained for TMTES, TIPS and PS mass spectra through a multivariate analysis approach.

Device Characterization: The OFETs were characterized by measuring their transfer and output characteristics, using an Agilent B1500A semiconductor device analyzer connected to the samples with a Karl SÜSS probe station, at ambient conditions.

The characteristic field-effect mobility (μ) and threshold voltage (V_{TH}) parameters were extracted in saturation regime using the following classic MOSFET equation:

$$\mu = \frac{2L}{WC}\left(\frac{\partial\sqrt{|I_{DS}|}}{\partial V_{GS}}\right)^2 \tag{1}$$

where C is insulator capacitance per unit area (C = 17.26 nF cm^{-2}), and W and L are the width and length of the channel, respectively. For each ink formulation, the devices parameters were extracted from at least 30 devices from two substrates to ensure thin film homogeneity and reproducibility.

The interfacial trap density for the majority charge carriers (i.e., holes) per unit area (N_T) was extracted directly to subthreshold swing (SS), and has been estimated using the following equations:

$$S = \left(\frac{\partial(\log I_{DS})}{\partial V_{GS}}\right)^{-1} \tag{2}$$

$$N_T \approx \frac{C}{q^2}\left[\frac{qSS}{k_B T \ln(10)} - 1\right] \tag{3}$$

where q is the electronic charge, k_B is the Boltzmann constant, and T is the absolute temperature.

During X-ray irradiation tests, the electrical photoresponse of the devices was measured by using a Keithley 2614 Source Meter, controlled by a customized Labview software. All measurements were carried out keeping the device in dark, in a Faraday cage, to reduce electrical noise and avoid light-induced photogeneration in the OSCs.

X-Ray Irradiation: Two different X-ray beam sources are employed for the characterization of the detectors: a) Hamamatsu L12161 X-ray tube with tungsten target was used at fixed 40 kV operating voltage the filament current was changed between 100 and 500 μA leading to an incident dose rate on the samples between 318 and 1665 μ Gy s^{-1}. The dose rate calibrations were previously performed employing the Barracuda radiation detector (RTI Group). The modulation of the beam was obtained with a mechanical lead shutter placed close to the X-ray tube window. Keithley SMU 2614 was used in combination with a LabVIEW program for electrical signal acquisition. b) A monochromatic and aligned synchrotron X-ray beam with energy of 12 keV and dose rate in the range 0.05–35 mGy s^{-1}. Synchrotron measurements are carried out at ELETTRA – Trieste, in the SYRMEP beamline that is equipped with an ionization chamber for real-time dose rate monitoring. In addition, precision slits and a CCD camera allow to focus the beam and to control the irradiated area of the samples.

Theoretical Calculations: The J_{HOMO} intermolecular electronic couplings (i.e., HOMO-HOMO transfer integrals) between all crystallographically independent pairs of nearby molecules in both TMTES polymorphs were calculated using DFT-based calculations employing the Gaussian code[63] Specifically, each pair was extracted from the crystal as an isolated dimer and its electronic structure evaluated employing a 6–31(d,p) double zeta polarized basis set and the B3YLP hybrid functional[64]. The possible effects of polarization-induced differences in on-site energy for each molecule in each pair[65,66] was taken into account using the fragment charge difference approach as implemented in the e-coupling server.[67]

Supporting Information

Supporting Information is available from the Wiley Online Library or from the author.

Acknowledgements

This work was funded by the Spanish Government within: research projects GENESIS PID2019-111682RB-I00 and RTI2018-095460-B-I00, the “Severo Ochoa” Programme for Centers of Excellence in R&D (FUNFUTURE CEX2019-000917-S) and the “María de Maeztu” program for Spanish Structures of Excellence (MDM-2017-0767). Funding was also provided by the Generalitat de Catalunya (2017-SGR-918, 2017-SGR13). A.T. acknowledges his FPU fellowship and is enrolled in the UAB Materials Science PhD program. C.M-D. acknowledges her Juan de la Cierva grant (ref. FJC2019-042161-I) from Ministerio de Ciencia e Innovación. I.F., A.C., B.F. and L.B. acknowledge funding from INFN through the CSN5 FIRE project. All the authors acknowledge Giuliana Tromba and Diego Dreossi at ELETTRA synchrotron in Trieste for hardware and software technical support during the experiments, in particular for the acquisition of X-ray image. R.S. acknowledges funding from MINECO under grant agreement CTQ2017-87773-P/AEI/FEDER.

Conflict of Interest

The authors declare no conflict of interest.

Data Availability Statement

The data that support the findings of this study are available from the corresponding author upon reasonable request.

Keywords

high performance, organic field-effect transistors, organic semiconductor blends, X-ray detectors, X-ray images

Received: March 15, 2022
Revised: May 11, 2022
Published online: June 22, 2022

---

[1] S. Demchyshyn, M. Verdi, L. Basiricò, A. Ciavatti, B. Hailegnaw, D. Cavalcoli, M. C. Scharber, N. S. Sariciftci, M. Kaltenbrunner, B. Fraboni, *Adv. Sci.* **2020**, *7*, 2002586.

[2] G. Lutz, *Semiconductor Radiation Detectors – Device Physics*, Springer-Verlag Berlin and Heidelberg GmbH & Co. KG, Heidelberg, Germany, **2007**.

[3] A. Sultana, A. Reznik, K. S. Karim, J. A. Rowlands, *Med. Phys.* **2008**, *35*, 4324.

[4] H. M. Thirimanne, K. D. G. I. Jayawardena, A. J. Parnell, R. M. I. Bandara, A. Karalasingam, S. Pani, J. E. Huerdler, D. G. Lidzey, S. F. Tedde, A. Nisbet, C. A. Mills, S. R. P. Silva, *Nat. Commun.* **2018**, *9*, 2926.

[5] K. D. G. I. Jayawardena, H. M. Thirimanne, S. F. Tedde, J. E. Huerdler, A. J. Parnell, R. M. I. Bandara, C. A. Mills, S. R. P. Silva, *ACS Nano* **2019**, *13*, 6973.

[6] M. P. A. Nanayakkara, L. Matjačić, S. Wood, F. Richheimer, F. A. Castro, S. Jenatsch, S. Züfle, R. Kilbride, A. J. Parnell, M. G. Masteghin, H. M. Thirimanne, A. Nisbet, K. D. G. I. Jayawardena, S. R. P. Silva, *Adv. Funct. Mater.* **2021**, *31*, 2008482.

[7] A. Ciavatti, T. Cramer, M. Carroli, L. Basiricò, R. Fuhrer, D. M. De Leeuw, B. Fraboni, *Appl. Phys. Lett.* **2017**, *111*, 183301.
[8] H. Li, X. Shan, J. N. Neu, T. Geske, M. Davis, P. Mao, K. Xiao, T. Siegrist, Z. Yu, *J. Mater. Chem. C* **2018**, *6*, 11961.
[9] J. Peng, K. Ye, Y. Xu, L. Cui, R. Li, H. Peng, Q. Lin, *Sensors Actuators, A Phys* **2020**, *312*, 112132.
[10] A. Ciavatti, R. Sorrentino, L. Basiricò, B. Passarella, M. Caironi, A. Petrozza, B. Fraboni, *Adv. Funct. Mater.* **2021**, *31*, 2009072.
[11] G. N. Ankah, P. Büchele, K. Poulsen, T. Rauch, S. F. Tedde, C. Gimmler, O. Schmidt, T. Kraus, *Org. Electron.* **2016**, *33*, 201.
[12] L. Basiricò, A. Ciavatti, T. Cramer, P. Cosseddu, A. Bonfiglio, B. Fraboni, *Nat. Commun.* **2016**, *7*, 13063.
[13] I. Temiño, L. Basiricò, I. Fratelli, A. Tamayo, A. Ciavatti, M. Mas-Torrent, B. Fraboni, *Nat. Commun.* **2020**, *11*, 2136.
[14] A. Ciavatti, L. Basiricò, I. Fratelli, S. Lai, P. Cosseddu, A. Bonfiglio, J. E. Anthony, B. Fraboni, *Adv. Funct. Mater.* **2019**, *29*, 1806119.
[15] F. G. del Pozo, S. Fabiano, R. Pfattner, S. Georgakopoulos, S. Galindo, X. Liu, S. Braun, M. Fahlman, J. Veciana, C. Rovira, X. Crispin, M. Berggren, M. Mas-Torrent, *Adv. Funct. Mater.* **2016**, *26*, 2379.
[16] I. Temiño, F. G. Del Pozo, M. R. Ajayakumar, S. Galindo, J. Puigdollers, M. Mas-Torrent, *Adv. Mater. Technol.* **2016**, *1*, 1600090.
[17] A. Tamayo, S. Hofer, T. Salzillo, C. Ruzié, G. Schweicher, R. Resel, M. Mas-Torrent, *J. Mater. Chem. C* **2021**, *9*, 7186.
[18] T. Salzillo, A. Campos, A. Babuji, R. Santiago, S. T. Bromley, C. Ocal, E. Barrena, R. Jouclas, C. Ruzie, G. Schweicher, Y. H. Geerts, M. Mas-Torrent, *Adv. Funct. Mater.* **2020**, *30*, 2006115.
[19] A. Campos, S. Riera-Galindo, J. Puigdollers, M. Mas-Torrent, *ACS Appl. Mater. Interfaces* **2018**, *10*, 15952.
[20] K. Zhang, T. Marszalek, P. Wucher, Z. Wang, L. Veith, H. Lu, H. J. Räder, P. M. Beaujuge, P. W. M. Blom, W. Pisula, *Adv. Funct. Mater.* **2018**, *28*, 1805594.
[21] J. Panidi, A. F. Paterson, D. Khim, Z. Fei, Y. Han, L. Tsetseris, G. Vourlias, P. A. Patsalas, M. Heeney, T. D. Anthopoulos, *Adv. Sci.* **2018**, *5*, 1700290.
[22] K. Zhao, O. Wodo, D. Ren, H. U. Khan, M. R. Niazi, H. Hu, M. Abdelsamie, R. Li, E. Q. Li, L. Yu, B. Yan, M. M. Payne, J. Smith, J. E. Anthony, T. D. Anthopoulos, S. T. Thoroddsen, B. Ganapathysubramanian, A. Amassian, *Adv. Funct. Mater.* **2016**, *26*, 1737.
[23] M. R. Niazi, R. Li, E. Qiang Li, A. R. Kirmani, M. Abdelsamie, Q. Wang, W. Pan, M. M. Payne, J. E. Anthony, D. M. Smilgies, S. T. Thoroddsen, E. P. Giannelis, A. Amassian, *Nat. Commun.* **2015**, *6*, 8598.
[24] M. B. Madec, J. J. Morrison, V. Sanchez-Romaguera, M. L. Turner, S. G. Yeates, *J. Mater. Chem.* **2009**, *19*, 6750.
[25] J. H. Lee, Y. Seo, Y. D. Park, J. E. Anthony, D. H. Kwak, J. A. Lim, S. Ko, H. W. Jang, K. Cho, W. H. Lee, *Sci. Rep.* **2019**, *9*, 21.
[26] M. Berteau-rainville, A. Tamayo, T. Leydecker, A. Pezeshki, E. Orgiu, M. Mas-Torrent, *Appl. Phys. Express* **2021**, *119*, 103301.
[27] D. J. Gundlach, J. E. Royer, S. K. Park, S. Subramanian, O. D. Jurchescu, B. H. Hamadani, A. J. Moad, R. J. Kline, L. C. Teague, O. Kirillov, C. A. Richter, J. G. Kushmerick, L. J. Richter, S. R. Parkin, T. N. Jackson, J. E. Anthony, *Nat. Mater.* **2008**, *7*, 216.
[28] T. Salzillo, N. Montes, R. Pfattner, M. Mas-Torrent, *J. Mater. Chem. C* **2020**, *8*, 15361.
[29] M. R. Niazi, R. Li, M. Abdelsamie, K. Zhao, D. H. Anjum, M. M. Payne, J. Anthony, D. M. Smilgies, A. Amassian, *Adv. Funct. Mater.* **2016**, *26*, 2371.
[30] S. Choi, F. A. Larrain, C. Y. Wang, C. Fuentes-Hernandez, W. F. Chou, B. Kippelen, *J. Mater. Chem. C* **2016**, *4*, 8297.
[31] S. Li, D. Guérin, K. Lmimouni, *Microelectron. Eng.* **2018**, *195*, 62.
[32] Z. A. Lamport, K. J. Barth, H. Lee, E. Gann, S. Engmann, H. Chen, M. Guthold, I. McCulloch, J. E. Anthony, L. J. Richter, D. M. DeLongchamp, O. D. Jurchescu, *Nat. Commun.* **2018**, *9*, 5130.
[33] A. Pérez-Rodríguez, I. Temiño, C. Ocal, M. Mas-Torrent, E. Barrena, *ACS Appl. Mater. Interfaces* **2018**, *10*, 7296.
[34] F. Leonardi, S. Casalini, Q. Zhang, S. Galindo, D. Gutiérrez, M. Mas-Torrent, *Adv. Mater.* **2016**, *28*, 10311.
[35] R. Hamilton, J. Smith, S. Ogier, M. Heeney, J. E. Anthony, I. McCulloch, J. Veres, D. D. C. Bradley, T. D. Anthopoulos, *Adv. Mater.* **2009**, *21*, 1166.
[36] G. R. Llorente, M. B. Dufourg-Madec, D. J. Crouch, R. G. Pritchard, S. Ogier, S. G. Yeates, *Chem. Commun.* **2009**, 3059.
[37] J. F. Chang, T. Sakanoue, Y. Olivier, T. Uemura, M. B. Dufourg-Madec, S. G. Yeates, J. Cornil, J. Takeya, A. Troisi, H. Sirringhaus, *Phys. Rev. Lett.* **2011**, *107*, 066601.
[38] S. Illig, A. S. Eggeman, A. Troisi, L. Jiang, C. Warwick, M. Nikolka, G. Schweicher, S. G. Yeates, Y. H. Geerts, J. E. Anthony, H. Sirringhaus, *Nat. Commun.* **2016**, *7*, 10736.
[39] S. Riera-Galindo, A. Tamayo, M. Mas-Torrent, *ACS Omega* **2018**, *3*, 2329.
[40] H. Chung, Y. Diao, *J. Mater. Chem. C* **2016**, *4*, 3915.
[41] V. Coropceanu, J. Cornil, D. A. da Silva Filho, Y. Olivier, R. Silbey, J. L. Brédas, *Chem. Rev.* **2007**, *107*, 926.
[42] R. Pfattner, S. T. Bromley, C. Rovira, M. Mas-Torrent, *Adv. Funct. Mater.* **2016**, *26*, 2256.
[43] G. Schweicher, V. Lemaur, C. Niebel, C. Ruzié, Y. Diao, O. Goto, W. Y. Lee, Y. Kim, J. B. Arlin, J. Karpinska, A. R. Kennedy, S. R. Parkin, Y. Olivier, S. C. B. Mannsfeld, J. Cornil, Y. H. Geerts, Z. Bao, *Adv. Mater.* **2015**, *27*, 3066.
[44] P. J. Skabara, J. B. Arlin, Y. H. Geerts, *Adv. Mater.* **2013**, *25*, 1948.
[45] A. Campos, N. Oxtoby, S. Galindo, R. Pfattner, J. Veciana, S. T. Bromley, C. Rovira, M. Mas-Torrent, *CrystEngComm* **2016**, *18*, 6149.
[46] K. L. Mccall, S. R. Rutter, E. L. Bone, N. D. Forrest, J. S. Bissett, J. D. E. Jones, M. J. Simms, A. J. Page, R. Fisher, B. A. Brown, S. D. Ogier, *Adv. Funct. Mater.* **2014**, *24*, 3067.
[47] M. M. Ibrahim, A. C. MacIel, C. P. Watson, M. B. Madec, S. G. Yeates, D. M. Taylor, *Org. Electron.* **2010**, *11*, 1234.
[48] A. Y. B. Meneau, Y. Olivier, T. Backlund, M. James, D. W. Breiby, J. W. Andreasen, H. Sirringhaus, *Adv. Funct. Mater.* **2016**, *26*, 2326.
[49] A. Tamayo, T. Salzillo, M. Mas-Torrent, *Adv. Mater. Interfaces* **2022**, *9*, 2101679.
[50] Y. Gao, Y. Ge, X. Wang, J. Liu, W. Liu, Y. Cao, K. Gu, Z. Guo, Y. M. Wei, N. Zhou, D. Yu, H. Meng, X. F. Yu, H. Zheng, W. Huang, J. Li, *Adv. Mater.* **2021**, *33*, 2101717.
[51] A. M. Zeidell, T. Ren, D. S. Filston, H. F. Iqbal, E. Holland, J. D. Bourland, J. E. Anthony, O. D. Jurchescu, *Adv. Sci.* **2020**, *7*, 2001522.
[52] S. Lai, P. Cosseddu, L. Basiricò, A. Ciavatti, B. Fraboni, A. Bonfiglio, *Adv. Electron. Mater.* **2017**, *3*, 1600409.
[53] L. Basiricò, A. Ciavatti, I. Fratelli, D. Dreossi, G. Tromba, S. Lai, P. Cosseddu, A. Bonfiglio, F. Mariotti, C. Dalla Val, V. Bellucci, J. E. Anthony, B. Fraboni, *Front. Phys.* **2020**, *8*, https://doi.org/10.3389/fphy.2020.00013.
[54] L. Mao, Y. Li, H. Chen, L. Yu, J. Zhang, *Nanomaterials* **2021**, *11*, 1832.
[55] H. M. Thirimanne, K. D. G. I. Jayawardena, A. Nisbet, Y. Shen, R. M. I. Bandara, C. A. Mills, G. Shao, S. R. P. Silva, *IEEE Trans. Nucl. Sci.* **2020**, *67*, 2238.
[56] J. Liu, B. Shabbir, C. Wang, T. Wan, Q. Ou, P. Yu, A. Tadich, X. Jiao, D. Chu, D. Qi, D. Li, R. Kan, Y. Huang, Y. Dong, J. Jasieniak, Y. Zhang, Q. Bao, *Adv. Mater.* **2019**, *31*, 1901644.
[57] J. Zhao, L. Zhao, Y. Deng, X. Xiao, Z. Ni, S. Xu, J. Huang, *Nat. Photonics* **2020**, *14*, 612.
[58] H. Tsai, F. Liu, S. Shrestha, K. Fernando, S. Tretiak, B. Scott, D. T. Vo, J. Strzalka, W. Nie, *Sci. Adv.* **2020**, *6*, eaay0815.
[59] H. Mescher, F. Schackmar, H. Eggers, T. Abzieher, M. Zuber, E. Hamann, T. Baumbach, B. S. Richards, G. Hernandez-Sosa, U. W. Paetzold, U. Lemmer, *ACS Appl. Mater. Interfaces* **2020**, *12*, 15774.
[60] J. Guo, Y. Xu, W. Yang, B. Xiao, Q. Sun, X. Zhang, B. Zhang, M. Zhu, W. Jie, *ACS Appl. Mater. Interfaces* **2021**, *13*, 23928.

[61] L. Basiricò, S. P. Senanayak, A. Ciavatti, M. Abdi-Jalebi, B. Fraboni, H. Sirringhaus, *Adv. Funct. Mater.* **2019**, *29*, 1902346.
[62] Pexraytech, Portable X-Ray Systems, Security Systems, https://pexraytech.com/security-systems/ 26th Febrary, **2022**.
[63] M. Frisch, G. Trucks, H. Schlegel, G. Scuseria, M. Robb, J. Cheeseman, G. Scalmani, V. Barone, G. Petersson, H. Nakatsuji, Gaussian09, Revis. D 1.
[64] P. J. Stephen, F. J. Devlin, C. F. Chabalowski, M. J. Frisch, *J. Phys. Chem.* **1994**, *98*, 11 623.
[65] K. Senthilkumar, F. C. Grozema, F. M. Bickelhaupt, L. D. A. Siebbeles, *J. Chem. Phys.* **2003**, *119*, 9809.
[66] E. F. Valeev, V. Coropceanu, D. A. Da Silva Filho, S. Salman, J. L. Brédas, *J. Am. Chem. Soc.* **2006**, *128*, 9882.
[67] I. Cabeza de Vaca, S. Acebes, V. Guallar, *J. Comput. Chem.* **2016**, *37*, 1740.